ACS APPLIED MATERIALS & INTERFACES

Research Article

www.acsami.org

Bandgap Engineering of Coal-Derived Graphene Quantum Dots

Ruquan Ye,[†] Zhiwei Peng,[†] Andrew Metzger,[†] Jian Lin,[‡,§,⊥] Jason A. Mann,[†] Kewei Huang,[†] Changsheng Xiang,[†] Xiujun Fan,[‡,§,∥] Errol L. G. Samuel,[†] Lawrence B. Alemany,[†,§,#] Angel A. Martí,*[,†,‡,§] and James M. Tour*[,†,‡,§]

[†]Department of Chemistry, [‡]Department of Materials Science and NanoEngineering, [§]Smalley Institute for Nanoscale Science and Technology, [#]Shared Equipment Authority, Rice University, 6100 Main Street, Houston, Texas 77005, United States

[⊥]Department of Mechanical & Aerospace Engineering, University of Missouri−Columbia, Columbia, Missouri 65211, United States

[∥]College of Electronic Information and Control Engineering, Beijing University of Technology, Beijing 100124, China

Supporting Information

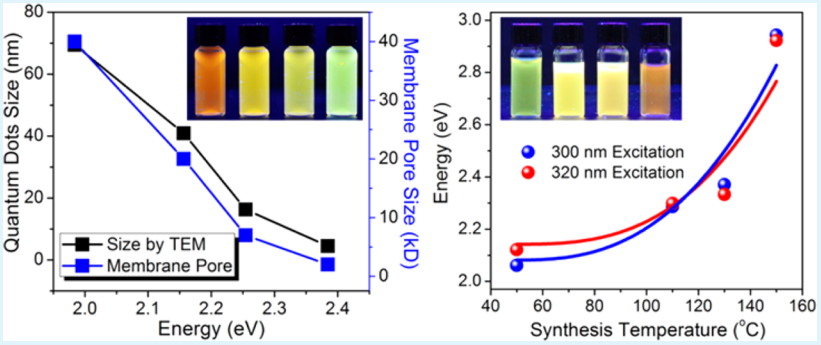

ABSTRACT: Bandgaps of photoluminescent graphene quantum dots (GQDs) synthesized from anthracite have been engineered by controlling the size of GQDs in two ways: either chemical oxidative treatment and separation by cross-flow ultrafiltration, or by a facile one-step chemical synthesis using successively higher temperatures to render smaller GQDs. Using these methods, GQDs were synthesized with tailored sizes and bandgaps. The GQDs emit light from blue-green (2.9 eV) to orange-red (2.05 eV), depending on size, functionalities and defects. These findings provide a deeper insight into the nature of coal-derived GQDs and demonstrate a scalable method for production of GQDs with the desired bandgaps.

KEYWORDS: *graphene quantum dots, bandgap, photoluminescent, anthracite, cross-flow filtration*

INTRODUCTION

Tailoring the bandgap of inorganic nanorods and quantum dots by confining the electrons in zero-dimensional (0-D) or one-dimensional (1-D) nanostructures has attracted tremendous research interest and found broad applications in various fields, such as photovoltaics,[1,2] biomedical and biological imaging[3,4] and as light-emitting sources.[5] Conventional methods of tuning the band structure of these materials include a variety of approaches, for example, laser molecular beam epitaxy growth of In_2O_3 nanoislands, supramolecular assembly of gold nanoparticles, epitaxial deposition of a compressive shell onto CdTe quantum dots, plasma-enhanced chemical vapor deposition of silicon quantum dots, and strain control of MoS_2 layers.[6−10] However, apart from the problems associated with these techniques that require specific and less accessible instruments or rigid reaction conditions, these inorganic quantum dots themselves are usually exceedingly expensive to prepare and they are sometimes toxic materials. This has limited their broader applications except in the cases where the toxicity has not been an issue or where the quantities required are minute.[4,11−13]

Although the long-studied inorganic quantum dots often have sharper emissions, luminescent carbon-based quantum dots sometimes show superior performance in terms of their high biocompatibility while remaining photostable.[14−17] Graphene quantum dots (GQDs) have been shown to have minimal toxicity.[18,19] Methods for preparing GQDs with specific bandgaps have been developed, for example, by chromatography with gradient elution of different mobile phases, cutting of tattered graphite using amines and element-doping of as-prepared GQDs.[20−22] However, complex separation techniques, multistep syntheses or high reagent costs have limited their scalable production.

Here we report a one-step and cost-effective method for the preparation of GQDs from coal. Formerly, we prepared GQDs with controlled bandgaps using a variety of coals that each possessed different-sized graphene domains.[23] However, here GQDs were prepared solely from anthracite coal, yet we

Received: February 12, 2015
Accepted: March 10, 2015
Published: March 10, 2015

DOI: 10.1021/acsami.5b01419
ACS Appl. Mater. Interfaces 2015, 7, 7041−7048

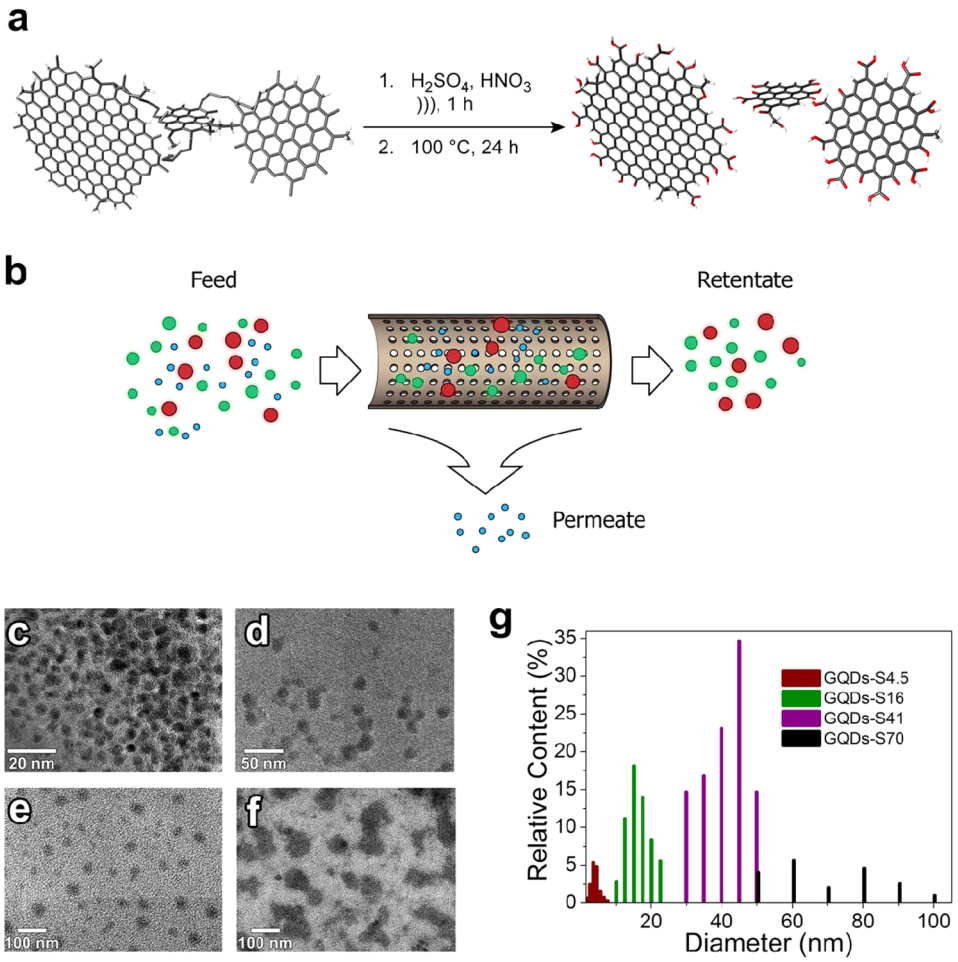

Figure 1. (a) Schematic illustration of GQD synthesis. (b) Schematic illustration of the separation of GQDs using cross-flow ultrafiltration. TEM images of the cross-flow ultrafiltration-separated (c) GQDs-S4.5, (d) GQDs-S16, (e) GQDs-S41 and (f) GQDs-S70. (g) Summary of size distributions of GQDs-S4.5, GQDs-S16, GQDs-S41 and GQDs-S70 determined by TEM.

control the bandgaps in two ways. In one case, the GQDs were rapidly purified using cross-flow ultrafiltration to separate them by size via variation of the membrane pore size. Such cross-flow ultrafiltration is used in very large-scale industrial processes for industrial and municipal water purification and for food separations.[24,25] The emission wavelengths of the purified GQDs depend on their sizes, in accord with the quantum confinement effect,[26] and on their functionalities and defects. In a second approach, instead of using ultrafiltration, we engineer the bandgaps of the GQDs by controlling the reaction temperature of the oxidation process, resulting in the synthesis of temperature-defined sizes of GQDs with fluorescence properties covering the visible spectrum. The higher the temperature, the smaller the GQDs, underscoring the facility with which the domain sizes could be controllable through oxidative cutting.

RESULT AND DISCUSSION

In the first reaction protocol, using an oxidative chemical reaction and the cross-flow ultrafiltration process, GQDs with different sizes were prepared. As shown in Figure 1a, raw anthracite is first dispersed in a mixed solvent of sulfuric acid and nitric acid, and then heated at a defined temperature for 24 h, which results in a clear solution. More details are provided in the Supporting Information. After purification, the GQD solution was processed with a cross-flow system (Figure 1b) using sequentially 3, 10 and 30 kD pore size membranes at ~1 atm transmembrane pressure (TMP).[24,25] Figure 1c–f shows the transmission electron microscopy (TEM) images of the as-separated GQDs; their corresponding sizes and hydrodynamic diameters obtained from TEM and dynamic light scattering (DLS) analyses are summarized in Figures 1g and S1 (Supporting Information), respectively. The size distribution in Figure 1g is statistically averaged from the TEM images with a sample size of ~150 particles. The distribution of hydrodynamic diameters was calculated from the light scattering in bulk solution. After the purification process, TEM images reveal that GQDs with average sizes of 4.5 ± 1.2, 16 ± 3.3, 41 ± 6.4 and 70 ± 15 nm were obtained, while the corresponding hydrodynamic diameters were 10 ± 2.5, 27 ± 7.9, 41 ± 11 and 76 ± 18 nm, respectively. The enlarged size in the DLS analyses was attributed to the hydration layers around the GQDs. The corresponding GQD batches are denoted as GQDs-S*x*, where "S" signifies "separated" and "*x*" indicates the average diameter from TEM images.

Two solid state NMR experiments employing magic angle spinning (MAS) were used to study the materials: direct ^{13}C pulse and ^{1}H-^{13}C cross-polarization (CP). The latter is normally sufficient for characterization of proton-rich materials, but for the materials studied here, with potentially large proton-deficient regions, the direct ^{13}C pulse approach was also used.[27] For each type of experiment, a survey spectrum was obtained

DOI: 10.1021/acsami.5b01419
ACS Appl. Mater. Interfaces 2015, 7, 7041−7048

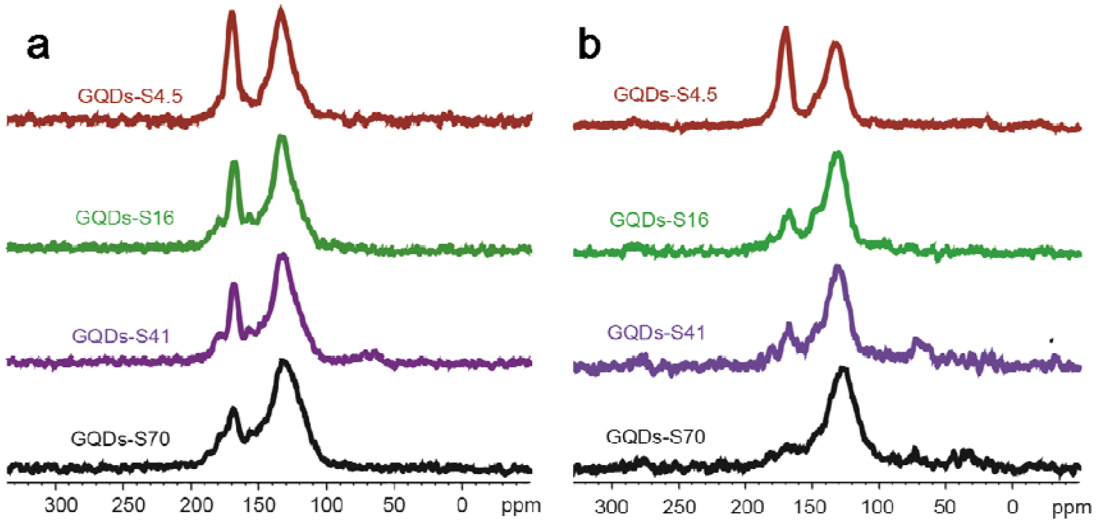

Figure 2. (a) Direct ^{13}C pulse MAS NMR and (b) cross-polarization ^{13}C MAS NMR spectra of GQDs-S4.5, GQDs-S16, GQDs-S41 and GQDs-S70. Experimental details are in the Supporting Information.

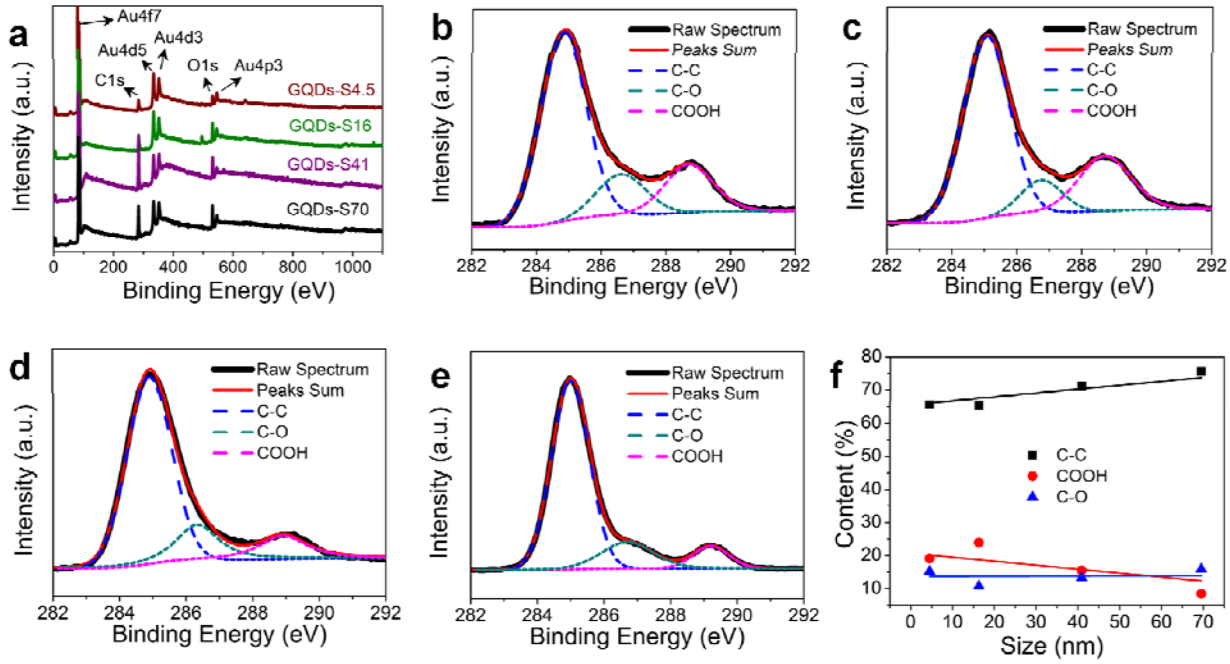

Figure 3. (a) XPS survey of GQDs-S4.5, GQDs-S16, GQDs-S41 and GQDs-S70 with Au as the reference. C 1s high resolution XPS spectra of (b) GQDs-S4.5, (c) GQDs-S16, (d) GQDs-S41 and (e) GQDs-S70. (f) Summary of percentage elemental contents in different functional groups from (b) to (e).

with a single set of parameters (Figure 2) in order to obtain at least qualitative information about each GQD sample. Each experiment reveals a prominent band with a peak maximum at ~130 ppm from aromatic and alkene groups. A signal at ~170 ppm, most likely from carbonyl groups, is also apparent in most spectra. For each sample, the relative intensities of the aromatic/alkene and carbonyl signals clearly differ in the direct ^{13}C pulse and CP spectra. Attempting quantitative interpretation would require CP spectra obtained at multiple contact times and direct ^{13}C pulse spectra obtained with multiple relaxation delays. Nevertheless, it is apparent from just these survey spectra that as the GQD size increases, the direct ^{13}C pulse spectra indicate that a much wider variety of carbonyl environments is generated, apparently including ketone as well as carboxyl functional groups, whereas the CP spectra indicate that the carbonyl groups in the larger GQDs do not cross polarize as well as in the smallest GQD. As the GQDs become larger, the relative content of carbonyl groups becomes smaller. Likewise, the effect of neighboring protons on peak intensity becomes small as the GQDs are larger. These results are consistent with the oxidized graphitic structure of coal-derived GQDs.[23]

The chemical structures of GQDs were further confirmed by X-ray photoelectron spectroscopy (XPS) analyses and Fourier transform infrared (FTIR) analyses. The XPS survey of GQDs of different sizes (Figure 3a) indicates that the GQDs primarily consist of carbon and oxygen. As shown in Figures 3b–e, the high resolution C 1s XPS spectra of GQDs show the presence

DOI: 10.1021/acsami.5b01419
ACS Appl. Mater. Interfaces 2015, 7, 7041–7048

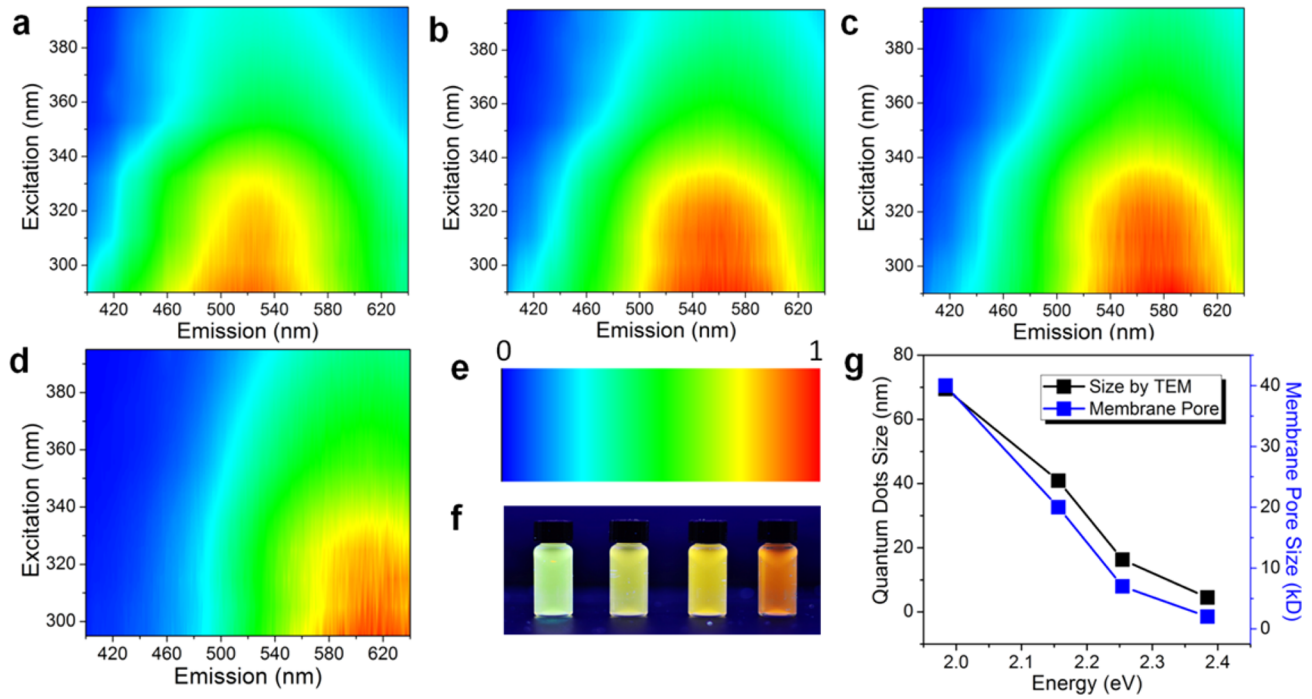

Figure 4. 2-D excitation−emission contour map of (a) GQDs-S4.5, (b) GQDs-S16, (c) GQDs-S41 and (d) GQDs-S70, all at ∼80 mg/L in water at pH 6. (e) Normalized intensity scale bar for panels a−d. (f) Solution of GQDs under 365 nm excitation UV lamp. The left-most vial is the GQDs-S4.5 solution, then GQDs-S16, GQDs-S41 and the right-most vial is the GQDs-S70 solution. (g) Relationship between the optical bandgap and GQD size (from TEM) or membrane pore sizes used in the ultrafiltration.

of COOH and C−O peaks at 288.8 and 286.6 eV, respectively. The relative abundances of these functionalities are summarized in Figure 3f. The quantitative assessment of relative aromatic/alkene to carbonyl ratios is not as descriptive as in the NMR experiments. In the FTIR spectra shown in Figure S2a−d (Supporting Information), C−H stretching modes appear at ∼2980 cm^{-1} in the small GQDs, whereas such functionality becomes less detectable as the size of the GQDs increases. This is attributed to the decreasing abundance of edge C−H stretching as the GQDs became larger. The carbonyl stretches are clearly seen, but assigning relative intensities between samples is difficult.

The effectiveness of separating GQDs by cross-flow ultrafiltration was further assessed by studying the photophysical properties of the separated GQDs. Figure S3 (Supporting Information) shows the UV−visible absorption of the GQDs. Larger GQDs tend to absorb at longer wavelengths, whereas the absorption of smaller GQDs is blue-shifted. The broad absorption of larger GQDs is attributed to the complexity of the electronic states. Figure 4a−e shows the 2-D excitation−emission contour maps of the GQDs. Under a 365 nm UV light, these quantum dots solutions emit light across the majority of the visible spectrum from green (∼2.4 eV) to orange-red (∼1.9 eV) regions (Figure 4f). The correlations between bandgap and size or molecular weight cutoff are summarized in Figure 4g. As expected, when the GQDs size increases from 4.5 to 70 nm, the peak emission is red-shifted from ∼520 to ∼620 nm, which is in accord with the quantum confinement effect.[26] These GQDs exhibit different fluorescent quantum yields of 1.1%, 0.89%, 0.65% and 0.38% using quinine sulfate as a reference standard, as the GQDs size increases from 4.5 to 70 nm. The decrease of quantum yield as the size increases suggests that the fluorescence is affected by the defects in the GQDs because the larger GQDs have fewer defect sites per unit area induced by oxidation and consequently become less emissive. The low quantum yields of these GQDs are similar to the published data.[20,28] As reported by Sun and co-workers,[29] a simple hydrothermal treatment in base improves the quantum yields. For example, heating GQDs-S4.5 in 0.2 M aqueous NaOH solution raises the quantum yield to 8.1% or 10%, in air or argon, respectively (Figure S4, Supporting Information). Similar enhancement was observed when treating GQDs in 1 M aqueous Na_2S at 100 °C for 1 d. For example, the quantum yield of GQDs-S4.5 increases by ∼2× after Na_2S treatment (Figure S4, Supporting Information).

The separation technique can efficiently produce GQDs with controlled sizes. For example, the relative yields of GQDs-S4.5, GQDs-S16, GQDs-S41 and GQDs-S70 were 8%, 30%, 52% and 10%, respectively. This represents a 1.6%, 6%, 10% and 2% yield by weight starting from anthracite, therefore an overall yield of GQDs being 20%.

The second method used to tailor the size of the GQDs samples was through direct synthesis techniques rather than separation. This simple method for the production of size-differentiated GQDs, in one step without cross-flow ultrafiltration, is based on control of the reaction temperature. The GQDs synthesized at different temperatures for 24 h are denoted as GQDs-T*x*-*y*, where "T" signifies "temperature", "*x*" indicates the synthesis temperature and "*y*" signifies the TEM-derived size. The higher temperature produces more oxidation and etches the GQDs into smaller sizes, leading to an enlarged bandgap. The change in GQD size is shown in the TEM images (Figure S5, Supporting Information), where the average diameter of the GQDs are 54 ± 7.2, 27 ± 3.8, 25 ± 5.0 and 7.6 ± 1.8 nm as the synthesis temperature rose from 50 to 110, 130, and 150 °C, respectively. The corresponding molecular weights of the GQDs peaks were 60, 49, 44 and 27 kD, as

DOI: 10.1021/acsami.5b01419
ACS Appl. Mater. Interfaces 2015, 7, 7041−7048

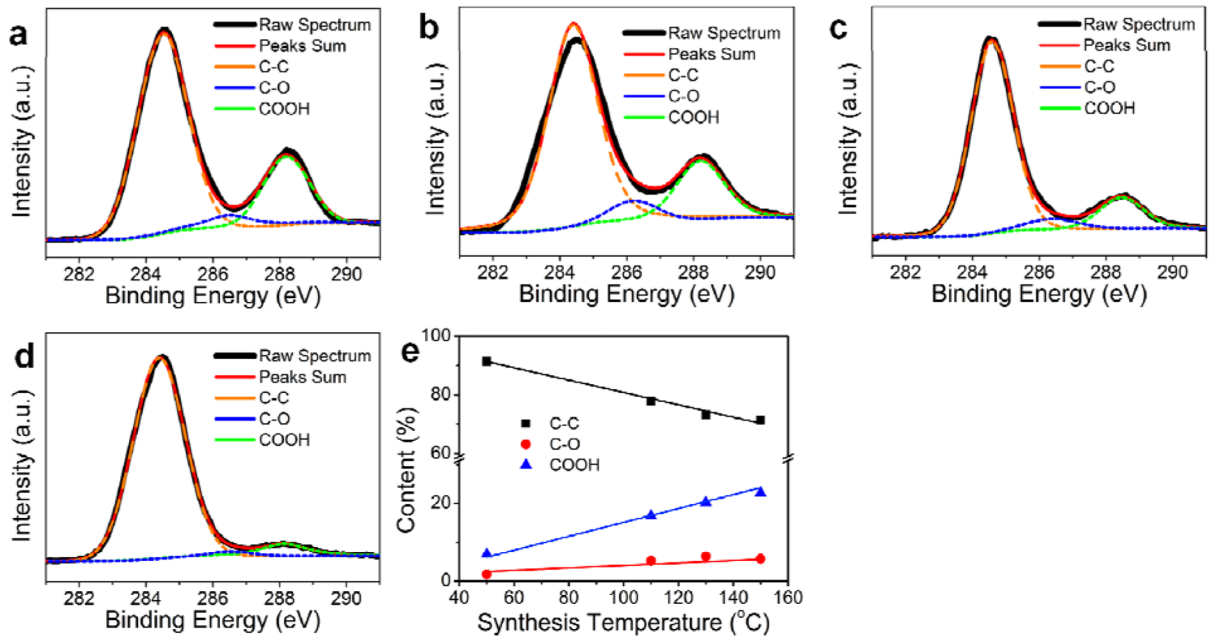

Figure 5. C 1s high resolution XPS spectra of (a) GQDs-T150-7.6, (b) GQDs-T130-25, (c) GQDs-T110-27 and (d) GQDs-T50-54. (e) Summary of percentage elemental contents in different functional groups from panels a to d.

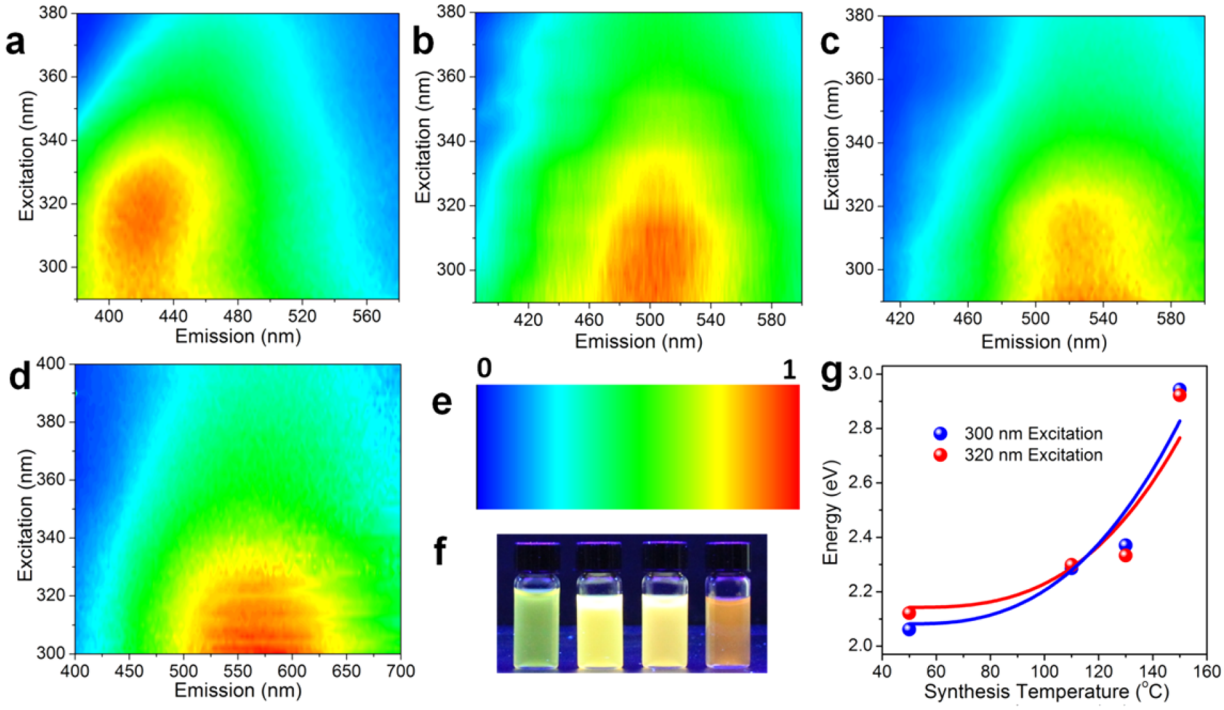

Figure 6. 2-D excitation−emission contour map of (a) GQDs-T150-7.6, (b) GQDs-T130-25, (c) GQDs-T110-27 and (d) GQDs-T50-54. The normalized scale bar is shown in panel e. The concentration is ∼30 mg/L at ∼pH 6. (f) GQDs solutions under 365 nm excitation UV lamp. The solutions from left to right are GQDs-T150-7.6, GQDs-T130-25, GQDs-T110-27 and GQDs-T50-54, respectively. (g) Summary of the peak intensities at 300 and 320 nm excitation wavelength from panels a to d.

determined by matrix-assisted laser desorption/ionization mass spectrometry (MALDI-MS, Figure S6, Supporting Information).

As expected, the diameters determined by TEM for the cross-flow ultrafiltered GQDs that were prepared at 100 °C fit well into the range of GQDs synthesized at different temperatures. This becomes more apparent when Figures 1g and S5e (Supporting Information) are made into a composite plot (Figure S7, Supporting Information). The functionality ratios on the GQDs also change with the synthesis temperature. Similar to the ^{13}C MAS NMR GQDs separated by cross-flow ultrafiltration, these GQDs synthesized at different temperatures show primarily the existence of carbonyl groups and aromatic/alkene groups at ∼170 and 130 ppm, respectively (Figure S8, Supporting Information). Raising the synthesis temperature to 150 °C apparently results in a more uniform

DOI: 10.1021/acsami.5b01419
ACS Appl. Mater. Interfaces 2015, 7, 7041−7048

structure, as the aromatic/alkene and carbonyl signals significantly sharpen. Differences between the direct ^{13}C pulse spectrum and the cross-polarization spectrum are particularly noticeable for GQDs-T110-27; in the direct ^{13}C pulse experiment, the aliphatic carbons apparently have very long ^{13}C spin−lattice relaxation times and thus give very weak signals. In the ^{1}H-^{13}C cross-polarization experiment, a much shorter ^{1}H spin−lattice relaxation time enables these aliphatic impurities, from various -O−C(sp^3) and -O−C(sp^3)−O- environments, to be much more readily detected. As shown in Figure 5a−e, the high resolution C 1s XPS spectra show that the percentage of COOH functionality increases from ∼4% to ∼22% and C−C bond content decreases from ∼93% to ∼65% as the synthesis temperature was increased from 50 to 150 °C. The corresponding changes in the NMR spectra (stronger signal near 170 ppm and reduced aromatic/alkene intensity) are qualitatively consistent with the XPS results. However, the noncarboxyl C−O content remained constant throughout the temperature range.

We further examined the UV−visible absorption and 2-D excitation−emission of GQDs synthesized at the different temperatures. The absorption spectra of GQDs synthesized at different temperatures (Figure S9, Supporting Information) are similar to the spectra of the GQDs prepared by cross-flow ultrafiltration. At higher synthesis temperatures, the absorption curve slopes abruptly in the low wavelength region, whereas at low synthesis temperatures, the absorption tends to be broad across the visible region. We further studied the control of the GQD bandgap through reaction temperature by analyzing the emission properties of GQDs. As shown in Figure 6a−e, the emission peak shifts from ∼580 to ∼420 nm as the temperature elevates from 50 to 150 °C, corresponding to the orange-red and blue-green emission color, respectively. The maximum excitation also shifts from ∼320 to ∼300 nm as the temperature decreases from 150 to 50 °C. This red-shift in maximum excitation is attributed to the narrowing of the bandgap at lower synthesis temperatures. The change in bandgap is visualized in Figure 6f, where the GQDs solutions under a 365 nm excitation UV lamp emit from blue-green to orange-red. The temperature effect in bandgap engineering of GQDs is summarized in Figure 6g. No apparent change occurs in the emission maxima as the excitation wavelength changes from 300 to 320 nm. An abrupt increase in bandgap is observed from 130 to 150 °C. As summarized in Figure 5e, the COOH content increases and the C−C content decreases at higher temperatures. The tunable bandgap of GQDs is attributed to both the size effect and functionality effect.[30,31] Because of the inherent smaller graphitic structure in bituminous coal,[23] direct synthesis of GQDs from bituminous coal with blue emission will be easier. As shown in Figure 7, GQDs extracted from bituminous coal at 120 °C emit blue light under a 365 nm UV lamp.

The effect of reaction time on tuning the bandgap of GQDs was also evaluated by studying the properties of GQDs synthesized at 130 °C with different reaction times. As shown in Figure S10 (Supporting Information), the peak emissions of GQDs reacted for 1 and 6 h show no apparent shift, indicating that the reaction time does not appreciably affect the emission maximum. Instead, the temperature is the determinant factor in tailoring the bandgap of GQDs. Furthermore, the facile control of the coal-derived GQD bandgaps is attributed to the intrinsically smaller 2-D crystalline domain sizes within the coal when compared to the domain sizes in graphite (Figure S11, Supporting Information) along with the product defects.

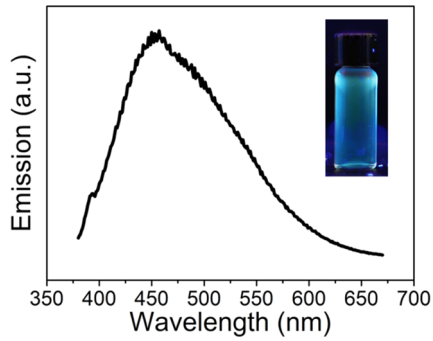

Figure 7. Emission spectrum of GQDs synthesized from bituminous coal at 120 °C; excited at 345 nm. Inset shows the GQDs solution under a 365 nm UV lamp.

CONCLUSION

We have developed two approaches to obtain GQDs with controlled bandgaps. One is using cross-flow ultrafiltration to separate GQDs by size, and the other is directly controlling the reaction temperature, which affects the final GQD size. These GQDs display photoluminescence, depending on size and functionalities, from green to orange-red. The tunable emission and fluorescence quantum yield indicates that the photoluminescence of GQDs derived from coal comes from the intrinsic state emission and defect state emission.[32−34] These effective and efficient approaches to tailoring the morphology of GQDs lead to materials that will be beneficial to a broad field of applications where sizes, edges and fluorescent band structures play an important role. For example, in bioimaging techniques, the fluorescence of the fluorophore could be engineered and enhanced to minimize the influence of the intrinsic fluorescence of cells;[35] in catalyst reactions, the activity of the catalytic could be increased by manipulating the edges of the GQDs;[36,37] in metal or chemical detection applications, the fluorescence wavelength could be tuned to avoid the interference of the metal or chemical emission.[38,39]

ASSOCIATED CONTENT

Supporting Information

Detailed procedure for synthesis and separation of GQDs, sample characterization and supplementary figures. This material is available free of charge via the Internet at http://pubs.acs.org.

AUTHOR INFORMATION

Corresponding Authors

*A. A. Martí. E-mail: amarti@rice.edu.

*J. M. Tour. E-mail: tour@rice.edu.

Notes

The authors declare no competing financial interest.

ACKNOWLEDGMENTS

This work was supported by the AFOSR (FA9550-14-1-0111) and the Robert A. Welch Foundation (C-1743).

REFERENCES

(1) Kongkanand, A.; Tvrdy, K.; Takechi, K.; Kuno, M.; Kamat, P. V. Quantum Dot Solar Cells. Tuning Photoresponse through Size and Shape Control of CdSe−TiO_2 Architecture. *J. Am. Chem. Soc.* **2008**, *130*, 4007.

DOI: 10.1021/acsami.5b01419
ACS Appl. Mater. Interfaces 2015, 7, 7041−7048

(2) Zhao, Q. D.; Xie, T. F.; Peng, L. L.; Lin, Y. H.; Wang, P.; Peng, L.; Wang, D. J. Size- and Orientation-Dependent Photovoltaic Properties of ZnO Nanorods. *J. Phys. Chem. C* **2007**, *111*, 17136.
(3) Klostranec, J. M.; Chan, W. C. W. Quantum Dots in Biological and Biomedical Research: Recent Progress and Present Challenges. *Adv. Mater.* **2006**, *18*, 1953.
(4) Zhao, X.; Wang, S. J.; Zhang, W. J.; Qiu, J. C.; Wu, Y. Z.; Liu, H. Z.; Xu, C. W.; Hao, X. P. Highly Biocompatible POSS-coated CdTe Quantum Dots for Cell Labeling. *RSC Adv.* **2014**, *4*, 598.
(5) Kim, J. H.; Holloway, P. H. Near-Infrared-Electroluminescent Light-Emitting Planar Optical Sources Based on Gallium Nitride Doped with Rare Earths. *Adv. Mater.* **2005**, *17*, 91−96.
(6) Zhang, K. H. L.; Bourlange, A.; Egdell, R. G.; Collins, S. P.; Bean, R. J.; Robinson, I. K.; Cowley, R. A. Size-Dependent Shape and Tilt Transitions in In_2O_3 Nanoislands Grown on Cubic Y-Stabilized ZrO_2(001) by Molecular Beam Epitaxy. *ACS Nano* **2012**, *6*, 6717.
(7) Daniel, M. C.; Astruc, D. Gold Nanoparticles: Assembly, Supramolecular Chemistry, Quantum-Size-Related Properties, and Applications toward Biology, Catalysis, and Nanotechnology. *Chem. Rev.* **2004**, *104*, 293.
(8) Smith, A. M.; Mohs, A. M.; Nie, S. Tuning the Optical and Electronic Properties of Colloidal Nanocrystals by Lattice Strain. *Nat. Nanotechnol.* **2009**, *4*, 56−63.
(9) Park, N. M.; Kim, T. S.; Park, S. J. Band Gap Engineering of Amorphous Silicon Quantum Dots for Light-Emitting Diodes. *Appl. Phys. Lett.* **2001**, *78*, 2575.
(10) Conley, H. J.; Wang, B.; Ziegler, J. I.; Haglund, R. F.; Pantelides, S. T.; Bolotin, K. I. Bandgap Engineering of Strained Monolayer and Bilayer MoS_2. *Nano Lett.* **2013**, *13*, 3626.
(11) Tang, Y.; Han, S. L.; Liu, H. M.; Chen, X.; Huang, L.; Li, X. H.; Zhang, J. X. The Role of Surface Chemistry in Determining *in Vivo* Biodistribution and Toxicity of CdSe/ZnS Core-Shell Quantum Dots. *Biomaterials* **2013**, *34*, 8741.
(12) Brunetti, V.; Chibli, H.; Fiammengo, R.; Galeone, A.; Malvindi, M. A.; Vecchio, G.; Cingolani, R.; Nadeau, J. L.; Pompa, P. P. InP/ZnS as a Safer Alternative to CdSe/ZnS Core/Shell Quantum Dots: *In Vitro* and *in Vivo* Toxicity Assessment. *Nanoscale* **2013**, *5*, 307.
(13) Soenen, S. J.; Rivera-Gil, P.; Montenegro, J. M.; Parak, W. J.; De Smedt, S. C.; Braeckmans, K. Cellular Toxicity of Inorganic Nanoparticles: Common Aspects and Guidelines for Improved Nanotoxicity Evaluation. *Nano Today* **2011**, *6*, 446.
(14) Liu, Q.; Guo, B. D.; Rao, Z. Y.; Zhang, B. H.; Gong, J. R. Strong Two-Photon-Induced Fluorescence from Photostable, Biocompatible Nitrogen-Doped Graphene Quantum Dots for Cellular and Deep-Tissue Imaging. *Nano Lett.* **2013**, *13*, 2436.
(15) Zhang, M.; Bai, L. L.; Shang, W. H.; Xie, W. J.; Ma, H.; Fu, Y. Y.; Fang, D. C.; Sun, H.; Fan, L. Z.; Han, M.; Liu, C. M.; Yang, S. H. Facile Synthesis of Water-Soluble, Highly Fluorescent Graphene Quantum Dots as a Robust Biological Label for Stem Cells. *J. Mater. Chem.* **2012**, *22*, 7461.
(16) Luk, C. M.; Tang, L. B.; Zhang, W. F.; Yu, S. F.; Teng, K. S.; Lau, S. P. An Efficient and Stable Fluorescent Graphene Quantum Dot−Agar Composite as a Converting Material in White Light Emitting Diodes. *J. Mater. Chem.* **2012**, *22*, 22378.
(17) Hu, C. F.; Liu, Y. L.; Yang, Y. H.; Cui, J. H.; Huang, Z. R.; Wang, Y. L.; Yang, L. F.; Wang, H. B.; Xiao, Y.; Rong, J. H. One-Step Preparation of Nitrogen-Doped Graphene Quantum Dots from Oxidized Debris of Graphene Oxide. *J. Mater. Chem. B* **2013**, *1*, 39.
(18) Chong, Y.; Ma, Y.; Shen, H.; Tu, X.; Zhou, X.; Xu, J.; Dai, J.; Fan, S.; Zhang, Z. The in Vitro and in Vivo Toxicity of Graphene Quantum Dots. *Biomaterials* **2014**, *35*, 5041.
(19) Nurunnabi, M.; Khatun, Z.; Huh, K. M.; Park, S. Y.; Lee, D. Y.; Cho, K. J.; Lee, Y. In Vivo Biodistribution and Toxicology of Carboxylated Graphene Quantum Dots. *ACS Nano* **2013**, *7*, 6858.
(20) Zhu, S. J.; Zhang, J. H.; Liu, X.; Li, B.; Wang, X. F.; Tang, S. J.; Meng, Q. N.; Li, Y. F.; Shi, C.; Hu, R.; Yang, B. Graphene Quantum Dots with Controllable Surface Oxidation, Tunable Fluorescence and up-Conversion Emission. *RSC Adv.* **2012**, *2*, 2717.
(21) Kwon, W.; Kim, Y. H.; Lee, C. L.; Lee, M.; Choi, H. C.; Lee, T. W.; Rhee, S. W. Electroluminescence from Graphene Quantum Dots Prepared by Amidative Cutting of Tattered Graphite. *Nano Lett.* **2014**, *14*, 1306.
(22) Tang, L.; Ji, R.; Li, X.; Bai, G.; Liu, C.; Hao, J.; Lin, J.; Jiang, H.; Teng, K. S.; Yang, Z.; Lau, S. P. Deep Ultraviolet to near-Infrared Emission and Photoresponse in Layered N-Doped Graphene Quantum Dots. *ACS Nano* **2014**, *8*, 6312−6320.
(23) Ye, R.; Xiang, C.; Lin, J.; Peng, Z.; Huang, K.; Yan, Z.; Cook, N. P.; Samuel, E. L.; Hwang, C. C.; Ruan, G.; Ceriotti, G.; Raji, A. R.; Marti, A. A.; Tour, J. M. Coal as an Abundant Source of Graphene Quantum Dots. *Nat. Commun.* **2013**, *4*, 2943.
(24) Muller, E. B.; Stouthamer, A. H.; Vanverseveld, H. W.; Eikelboom, D. H. Aerobic Domestic Waste Water Treatment in a Pilot Plant with Complete Sludge Retention by Cross-Flow Filtration. *Water. Res.* **1995**, *29*, 1179.
(25) Daufin, G.; Escudier, J. P.; Carrere, H.; Berot, S.; Fillaudeau, L.; Decloux, M. Recent and Emerging Applications of Membrane Processes in the Food and Dairy Industry. *Food Bioprod. Process.* **2001**, *79*, 89.
(26) Alivisatos, A. P. Semiconductor Clusters, Nanocrystals, and Quantum Dots. *Science* **1996**, *271*, 933.
(27) Conte, P.; Piccolo, A.; van Lagen, B.; Buurman, P.; Hemminga, M. A. State of the Art of CPMAS ^{13}C-NMR Spectroscopy Applied to Natural Organic Matter. *Solid State Nucl. Magn. Reson.* **2002**, *21*, 158.
(28) Shen, J.; Zhu, Y.; Yang, X.; Li, C. Graphene Quantum Dots: Emergent Nanolights for Bioimaging, Sensors, Catalysis and Photovoltaic Devices. *Chem. Commun.* **2012**, *48*, 3686−3699.
(29) Sun, H.; Gao, N.; Wu, L.; Ren, J.; Wei, W.; Qu, X. Highly Photoluminescent Amino-Functionalized Graphene Quantum Dots Used for Sensing Copper Ions. *Chem.—Eur. J.* **2013**, *19*, 13362−13368.
(30) Kumar, G. S.; Roy, R.; Sen, D.; Ghorai, U. K.; Thapa, R.; Mazumder, N.; Saha, S.; Chattopadhyay, K. K. Amino-Functionalized Graphene Quantum Dots: Origin of Tunable Heterogeneous Photoluminescence. *Nanoscale* **2014**, *6*, 3384−3391.
(31) Kim, S.; Hwang, S. W.; Kim, M.; Shin, D. Y.; Shin, D. H.; Kim, C. O.; Yang, S. B.; Park, J. H.; Hwang, E.; Choi, S.; Ko, G.; Sim, S.; Sone, C.; Choi, H. J.; Bae, S.; Hong, B. H. Anomalous Behaviors of Visible Luminescence from Graphene Quantum Dots: Interplay between Size and Shape. *ACS Nano* **2012**, *6*, 8203.
(32) Zhang, Z.; Zhang, J.; Chen, N.; Qu, L. Graphene Quantum Dots: An Emerging Material for Energy-Related Applications and beyond. *Energy Environ. Sci.* **2012**, *5*, 8869−8890.
(33) Lingam, K.; Podila, R.; Qian, H.; Serkiz, S.; Rao, A. M. Evidence for Edge-State Photoluminescence in Graphene Quantum Dots. *Adv. Funct. Mater.* **2013**, *23*, 5062−5065.
(34) Zhou, X.; Zhang, Y.; Wang, C.; Wu, X.; Yang, Y.; Zheng, B.; Wu, H.; Guo, S.; Zhang, J. Photo-Fenton Reaction of Graphene Oxide: A New Strategy to Prepare Graphene Quantum Dots for DNA Cleavage. *ACS Nano* **2012**, *6*, 6592−6599.
(35) Nurunnabi, M.; Khatun, Z.; Huh, K. M.; Park, S. Y.; Lee, D. Y.; Cho, K. J.; Lee, Y. *In Vivo* Biodistribution and Toxicology of Carboxylated Graphene Quantum Dots. *ACS Nano* **2013**, *7*, 6858−6867.
(36) Liu, Y.; Wu, P. Graphene Quantum Dot Hybrids as Efficient Metal-Free Electrocatalyst for the Oxygen Reduction Reaction. *ACS Appl. Mater. Interfaces* **2013**, *5*, 3362−3369.
(37) Fei, H.; Ye, R.; Ye, G.; Gong, Y.; Peng, Z.; Fan, X.; Samuel, E. L.; Ajayan, P. M.; Tour, J. M. Boron- and Nitrogen-Doped Graphene Quantum Dots/Graphene Hybrid Nanoplatelets as Efficient Electrocatalysts for Oxygen Reduction. *ACS Nano* **2014**, *8*, 10837−10843.
(38) Li, L.; Wu, G.; Hong, T.; Yin, Z.; Sun, D.; Abdel-Halim, E. S.; Zhu, J. Graphene Quantum Dots as Fluorescence Probes for Turn-off Sensing of Melamine in the Presence of Hg^{2+}. *ACS Appl. Mater. Interfaces* **2014**, *6*, 2858−2864.
(39) Zhou, X.; Wang, A.; Yu, C.; Wu, S.; Shen, J. Facile Synthesis of Molecularly Imprinted Graphene Quantum Dots for the Determi-

DOI: 10.1021/acsami.5b01419
ACS Appl. Mater. Interfaces 2015, 7, 7041−7048

nation of Dopamine with Affinity-Adjustable. *ACS Appl. Mater. Interfaces* **2015**, DOI: 10.1021/am5078478.

DOI: 10.1021/acsami.5b01419
ACS Appl. Mater. Interfaces 2015, 7, 7041−7048